



# Composites derived from exfoliated Laponite and Mn-Al hydrotalcite prepared in inverse microemulsion: A new strategy for design of robust VOCs combustion catalysts

Bogna D. Napruszewska<sup>a</sup>, Alicja Michalik-Zym<sup>a</sup>, Roman Dula<sup>a</sup>, Elżbieta Bielańska<sup>a</sup>, Wojciech Rojek<sup>a</sup>, Tadeusz Machej<sup>a</sup>, Robert P. Socha<sup>a</sup>, Lidia Lityńska-Dobrzyńska<sup>b</sup>, Krzysztof Bahranowski<sup>c</sup>, Ewa M. Serwicka<sup>a,\*</sup>

<sup>a</sup> Jerzy Haber Institute of Catalysis and Surface Chemistry, Niezapominajek 8, 30-239 Krakow, Poland

<sup>b</sup> Institute of Metallurgy and Materials Science, Polish Academy of Sciences, Reymonta 25, 30-059 Krakow, Poland

<sup>c</sup> AGH University of Science and Technology, Faculty of Geology, Geophysics and Environmental Protection, al. Mickiewicza 30, 30-059 Krakow, Poland

## ARTICLE INFO

### Article history:

Received 1 March 2017

Received in revised form 6 April 2017

Accepted 10 April 2017

Available online 12 April 2017

### Keywords:

Combustion catalysts

Clay/hydrotalcite composite

Mn oxides

Inverse micelle

Laponite

## ABSTRACT

A novel strategy of designing combustion catalysts is proposed, in which catalytically active oxide nanoparticles, obtained by inverse microemulsion method, are trapped between randomly oriented clay layers. MnAl hydrotalcite-like compound was used as the precursor of the active phase, while synthetic smectite Laponite RD, either in sodium form (Na-L) or as an organoclay, exchanged with cetyltrimethylammonium cations (CTA-L), served as the clay component. The composite catalysts were characterized with XRF, XRD, SEM, TEM/HRTEM, TG/DSC, H<sub>2</sub>TPR, XPS, and N<sub>2</sub> adsorption/desorption at -196 °C. It was found that the degree of clay exfoliation was higher in materials obtained from CTA-L than in the catalysts prepared from Na-L. In organo-Laponite based composites the MnO<sub>x</sub> particles were smaller, more uniform, and better dispersed. Upon calcination they evolved towards well ordered, slightly oxygen-rich Mn<sub>3</sub>O<sub>4</sub> nanocrystals, while in Na-L derived catalysts the MnO<sub>x</sub> grains were structurally less ordered and size-wise more diversified, of average oxidation state significantly higher than that characteristic of Mn<sub>3</sub>O<sub>4</sub>. All synthesized materials were highly active in combustion of toluene. Performance of composites based on Na-L was more susceptible to thermal degradation, while the organoclay-based catalysts improved their performance on the increase of the calcination temperature, showing eventually superior activity. The observed dependencies are discussed in terms of structure-composition-performance relationship. It is argued that, on one hand, the use of organoclay facilitates dispersion of the precursor micelles between the clay layers and prevents the occurrence of active phase coalescence, on the other, provides interlayer fuel for the additional heat input during calcination, enabling formation of well ordered, uniform, Mn<sub>3</sub>O<sub>4</sub> nanocrystals with oxygen-rich surface of unique redox and catalytic properties. The obtained results demonstrate the potential of using organoclays as supports for the active oxide phase prepared from inverse micellar precursors.

© 2017 Elsevier B.V. All rights reserved.

## 1. Introduction

Catalytic combustion is one of the most attractive ways of controlling the emission of volatile organic compounds (VOCs). Among non-noble metal catalysts designed for this purpose, those based on MnO<sub>x</sub> active phase have attracted particular interest due to high activity in total oxidation, durability, low cost and low toxicity

[1–3]. Hydrotalcite-like compounds, known to produce upon thermal decomposition oxide phases of unique properties [4] have been frequently used for manufacturing of Mn-containing combustion catalysts [5–18]. Mn oxides in combination with pillared smectite clays have also been found active in total oxidation processes [19–22]. The key challenge in the preparation of a successful transition metal oxide combustion catalyst is to find means to maximize the dispersion of the oxide active phase while simultaneously stabilizing it against thermal degradation resulting from sintering and solid state reactions with the support and within the active phase itself [23–25]. We decided to meet this challenge by designing inno-

\* Corresponding author.

E-mail address: [ncserwic@cyf-kr.edu.pl](mailto:ncserwic@cyf-kr.edu.pl) (E.M. Serwicka).

utive catalysts, in which catalytically active oxide nanoparticles, obtained by inverse microemulsion method, are trapped within a house of cards structure formed by the exfoliated smectite clay layers. MnAl hydrotalcite-like compound was chosen as precursor of the active phase. The advantage of employing inverse microemulsion method for the precursor synthesis has been indicated by Li et al. [26], who found that Mn-containing catalysts obtained in such a way were characterized by good dispersion of the active phase and high catalytic activity in oxidation of toluene. The use of inverse hydrotalcite-containing microemulsion in combination with clay for the catalyst design is a completely new approach. Introduction of clay component was intended to provide structural elements capable of separating/trapping the active phase nanoparticles, thus hindering the catalyst sintering-induced deactivation. The use of chemically inert layered silicate (Laponite) was expected to help to preserve the nanoparticle chemical identity in contact with the support. Moreover, the study addresses the influence of the Laponite interlayer cation (sodium or cetyltrimethylammonium) on the outcome of catalyst design. Composite catalysts activity is tested in the total oxidation of toluene.

## 2. Experimental

### 2.1. Materials

MnAl(3:1) hydrotalcite-like nanoparticles were prepared following the double-microemulsion method proposed by Bellezza et al. [27]. Two inverse microemulsions of hydrotalcite-forming reagents were prepared. In the first case, aqueous solution to be dispersed in the organic medium contained  $\text{Mn}(\text{NO}_3)_2$  (concentration 0.375 M) and  $\text{Al}(\text{NO}_3)_3$  (concentration 0.125 M), in the other it contained ammonia (concentration 3 M). Each was dispersed in the organic medium based on isoctane as oil phase, cetyltrimethylammonium bromide (CTABr) as surfactant, and *n*-butanol as co-surfactant. For each microemulsion the applied proportions were: 3.4 ml aqueous phase/3.12 g CTABr/4.81 g *n*-butanol/6.21 g isoctane. Equal volumes of the two microemulsions were mixed and aged at 70 °C for 16 h to enable precipitation of the hydrotalcite-like phase, referred to as MnAl(im). Further treatment varied, depending whether aqueous or organic route of hydrotalcite-clay composites synthesis was pursued. Synthetic smectite Laponite RD (Rockwood Additives Ltd. UK), with an empirical formula  $\text{Na}_{0.7}[\text{Si}_8\text{Mg}_{5.5}\text{Li}_{0.3}\text{O}_{20}(\text{OH})_4]$ , was used as the clay component. In the case of aqueous route, the MnAl(im) precipitate was recovered by centrifugation, washed with ethanol-chloroform mixture (1:1 v/v), then with water, and mixed with the sodium form of Laponite (Na-L) dispersed in 200 ml water. It has been noted that separation from the mother liquor and washing with water enhanced tendency to form agglomerates within the MnAl(im) precipitate. After vigorous stirring at 20 °C the composite catalyst precursors were filtered off and dried by lyophilization. Freeze-drying was employed in order to eliminate the effect of surface tension of the liquid medium. Organic route required transformation of the Na-L clay into an organic derivative by a routine cation exchange procedure with the CTABr aqueous solution. The cation-exchanged form, referred to as CTA-L, was centrifuged free of  $\text{Br}^-$  with distilled water, followed by washing with isopropanol. Then the organoclay was dispersed in 200 ml of isopropanol and added to the as received MnAl(im) suspension in organic mother liquor. After vigorous stirring at 20 °C the composite catalyst precursors were filtered off and lyophilized. For each preparative route three catalysts of different MnAl(im) content were obtained, the intended loadings corresponding approximately to 1:6, 1:3 and 1:2 MnAl(im)/clay weight ratios. For the 1:2 MnAl(im):Laponite loading the whole lot of MnAl(im) obtained from a single synthesis was used, while for

two other catalysts, the MnAl(im) batch was divided in two parts, in 1:2 wt ratio, and mixed with the same mass of clay, which resulted in 1:6 and 1:3 loading of MnAl(im) onto Laponite. In order to test the resistance of synthesized composites to thermal degradation, two series of catalysts were obtained: one calcined for 4 h at 450 °C, the other calcined for 4 h at 600 °C. In addition, a reference composite catalyst was prepared from the MnAl(3:1) hydrotalcite obtained by the standard co-precipitation method at pH = 10, referred to as MnAl(st). After washing with distilled water, the MnAl(st) aqueous suspension was added to the aqueous dispersion of Na-L in 1:6 wt ratio, stirred vigorously, filtered off, lyophilized and calcined at 600 °C for 4 h. The catalysts were denoted MnAl(im)/Na-L(x)-temp and MnAl(im)/CTA-L(x)-temp, for aqueous and organic route, respectively, where "x" was I, II, or III depending on the load of MnAl(im) component, and "temp" was the temperature of calcination, i.e. the sample signature MnAl(im)/Na-L(II)-450 means that the catalyst was obtained by the aqueous route, contains intermediate loading of MnAl(im) component and was calcined at 450 °C. Reference catalyst was denoted MnAl(st)/Na-L(I)-600.

### 2.2. Methods

X-ray diffraction (XRD) patterns were recorded using PANalytical X'Pert PRO MPD powder diffractometer with  $\text{CuK}\alpha$  radiation.

Chemical composition of investigated solids was determined with a ZSX Primus II Rigaku spectrometer with a Rh anode as X-ray source, using calibration based on certified reference materials.

High magnification SEM images were recorded for the uncoated samples deposited on 200 Mesh copper grids covered with carbon support film, using a JEOL JSM-7500F Field Emission Scanning Electron Microscope (SEM).

Transmission electron microscopic (TEM/HRTEM) studies were carried out with aid of FEI Tecnai G2 high resolution transmission electron microscope. For the measurements the samples were embedded in the epoxy resin and cut with the LEICA EMUC6 microtome into ultrathin sections.

X-ray Photoelectron Spectroscopy (XPS) spectra were obtained with a hemispherical analyzer (SES R4000, Gammasdata Scienta) and Mg K $\alpha$  X-ray source (1253.7 eV). The system was calibrated according to ISO 15472:2010. The electron binding energy scale (BE) was calibrated for C 1 s core excitation at 285.0 eV. The spectra were fitted with the Casa XPS 2.3.15 software, using Gaussian/Lorentzian functional (70:30) and Shirley-type background.

Temperature programmed reduction (TPR) was performed in a quartz U-shaped tubular reactor. About 0.015 g of sample was used. The reducing gas was a mixture of 5 vol.%  $\text{H}_2$  in Ar (Linde,  $\text{H}_2$  5% in Ar), at a total flow rate of 30 ml min $^{-1}$ . The temperature was increased at a rate of 10 °C min $^{-1}$  from room temperature to 650 °C. The TPR profiles were recorded using a thermal conductivity detector (TCD).

Textural parameters were derived from  $\text{N}_2$  adsorption/desorption measurements performed at –196 °C with the use of Quantachrome AUTOSORB 1 instrument. Prior to the measurement the samples were outgassed at 200 °C for 3 h. Specific surface areas were calculated according to the Brunauer–Emmett–Teller method ( $S_{\text{BET}}$ ) in the relative pressure range 0.02–0.04. The micropore surface area ( $S_{\text{micro}}$ ) and micropore volume ( $V_{\text{micro}}$ ) were determined by *t*-plot analysis. The total pore volume ( $V_{\text{tot}}$ ) was calculated from the amount of  $\text{N}_2$  adsorbed at a relative vapor pressure  $p/p_0 = 0.996$ . The mean diameters of all pores ( $D^{\text{av}}$ ) was evaluated using the Gurvitch formula  $D^{\text{av}} = 4V_{\text{tot}}/S_{\text{BET}}$ .

Catalytic combustion of toluene was carried out in a fixed-bed flow quartz reactor of 10 mm inner diameter, loaded with ca. 0.5 g of a catalyst (particle size 0.3–0.5 mm), in the temperature range 100–400 °C. Toluene at 500 ppm concentration was fed to the flow by passing air through a saturator, at GHSV of 10 000 h $^{-1}$ . The only

**Table 1**

XRF determined chemical composition (non-oxygen elements) of MnAl(im)/Na-L, MnAl(im)/CTA-L and reference catalyst, and XPS data on the relative content and oxidation state of surface Mn species of selected samples (AOS – average oxidation state), (\*bulk values in parentheses).

Sample	Si [at.%]	Mg [at.%]	Na [at.%]	Al [at.%]	Mn [at.%]	bulk Mn/Al	Mn <sup>2+</sup> [%]	Mn <sup>3+</sup> [%]	Mn <sup>4+</sup> [%]	surface Mn/Al	surface Mn/Si	Surface Mn AOS
MnAl(im)/Na-L(I)-600	49.5	33.9	3.1	3.4	10.1	2.97	13	69	18	0.20	0.03	3.1
MnAl(im)/Na-L(II)-600	44.2	29.8	2.7	5.9	17.4	2.95	15	61	24	0.30	0.05	3.1
MnAl(im)/Na-L(III)-600	36.8	25.2	2.1	8.9	27.0	3.03	n.d.	n.d.	n.d.	n.d.	n.d.	n.d.
MnAl(im)/CTA-L(I)-600	52.0	35.0	–	3.3	9.7	2.94	33	55	12	0.55	0.11	(0.19)
MnAl(im)/CTA-L(II)-600	46.7	31.4	–	5.5	16.4	2.98	26	59	15	0.78	0.18	2.9
MnAl(im)/CTA-L(III)-600	36.6	25.0	–	9.7	28.7	2.96	n.d.	n.d.	n.d.	n.d.	n.d.	n.d.
MnAl(st)/Na-L(I)-600	49.3	33.4	3.2	3.6	10.5	2.92	n.d.	n.d.	n.d.	n.d.	n.d.	n.d.

reaction products were CO<sub>2</sub> and water. Toluene consumption was measured by GC-FID (SRI 8610A) and CO<sub>2</sub> evolution by GC-HID (SRI 310). Variation of conversion values in repeated catalytic runs over the same catalyst sample was within a margin of  $\pm 0.5\%$ .

### 3. Results and discussion

#### 3.1. Characterization of catalysts

##### 3.1.1. Composition, structure, morphology and texture

The chemical composition of the investigated catalysts is shown in **Table 1**. The main difference between the materials obtained by aqueous route, as opposed to the organic one, is that the latter, derived from CTA-exchanged Laponite, contain no sodium. The Mn/Al ratio is close to the intended Mn/Al = 3 stoichiometry. No traces of bromine were found in the materials calcined in either of the employed temperatures.

Comparison of XRD patterns recorded for the active phase precursors obtained by inverse micelle and standard co-precipitation methods, respectively, shows that both samples display series of reflexes characteristic of a Mn-Al hydrotalcite-like phase, whose indexing, indicated for the better resolved MnAl(st) pattern, is based on the reported data (charmarite, Ref. code 00-051-1526) (**Fig. 1**). The hydrotalcite-like phase formed within micelles is of much lower crystallinity than the one obtained by the standard procedure, but all most intense reflexes of the hydrotalcite structure are observed. High magnification SEM images of uncoated MnAl(im) and MnAl(st), shown in **Fig. 2a** and b, respectively, reveal that although both materials display plate-like morphology, the pretty uniform hydrotalcite particles, with lateral dimensions of

ca. 30 nm, obtained by inverse microemulsion method, are much finer than those produced in a conventional manner. The effect reflects the impact of spatial constraints exerted by the limited volume of inverse micelles, as opposed to the unhindered precipitation conditions accompanying the standard co-precipitation procedure. The MnAl(st) precipitate contains some MnCO<sub>3</sub> impurity (rhombochrosite, Ref. code 04-001-7250), which is common for carbonate forms of Mn-Al hydrotalcite-like materials obtained by co-precipitation [28]. Noteworthy, the MnCO<sub>3</sub> impurity is absent in the MnAl(im) sample. This suggests that the hydrotalcite-like phase obtained by inverse microemulsion method is capable of accommodating more manganese than the material obtained by the standard route. Indeed, analysis of the XRD pattern around  $2\Theta = 60^\circ$  (insert in **Fig. 1**) shows that in MnAl(im) the (110) and (113) reflections are slightly shifted towards lower angles, in accordance with the presumed larger content of Mn<sup>2+</sup>, whose ionic radius in octahedral coordination (0.083 nm, high spin configuration) is larger than that of Al<sup>3+</sup> (0.054 nm). In the hydrotalcite-like phase prepared by inverse microemulsion the d<sub>003</sub> value is 0.789 nm, i.e. slightly higher than in the hydrotalcite component prepared by the standard procedure (0.753 nm), both values falling in the range characteristic of carbonate forms [28]. However, while in the case of the standard co-precipitation method, carbonate is the anion of preference, in the case of hydrotalcite-like phases synthesized by inverse micellar route, bromides, provided by the CTABr surfactant, are present in the reaction environment [27]. The expected d<sub>003</sub> value for bromide form of a hydrotalcite-like compound is around 0.8 nm [27,29], hence the d<sub>003</sub> observed for MnAl(im) points to the contribution of Br<sup>-</sup> as interlayer species.

XRD diagrams of composites calcined at 450 and 600 °C are gathered in **Fig. 3**. In addition, the patterns of individual components, Na-L and MnAl(im), are shown, to facilitate identification of reflections associated with various parts of the composites. The Na-L-450 clay sample shows pattern characteristic of Laponite (Ref. code 09-0031) with thermally collapsed interlayer, as indicated by the d<sub>001</sub> value around 1.01 nm. A similar pattern is given by Na-L calcined at 600 °C. The MnAl(im)-450 active phase is practically amorphous, while the MnAl(im)-600 material shows reflections characteristic of Mn<sub>3</sub>O<sub>4</sub>, hausmannite (Ref. code 00-024-0734). Analysis of XRD patterns produced by composite samples shows that features characteristic of calcined Laponite are visible in all materials. It should be noted that a completely exfoliated clay with a house of cards structure is not expected to give the (001) reflection, therefore its appearance in the composite materials indicates that partial restacking of clay layers occurred. The lower the intensity of this reflection for a given Laponite content, the higher is the degree of clay exfoliation. Intensity of Laponite reflections depends not only on the absolute clay content, but also on the manner of composite preparation. For the comparable MnAl(im)/clay ratio, the (001) reflection of Laponite is more pronounced in composites prepared from Na-L than in those derived from the organoclay. This

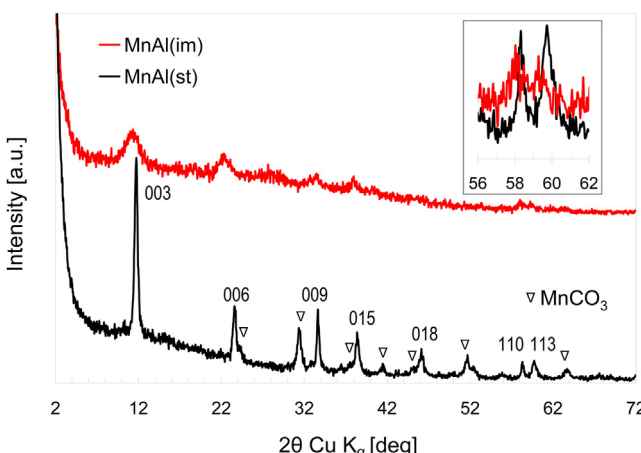


**Fig. 1.** XRD patterns of as received MnAl(im) and MnAl(st). Indexing of hydrotalcite-like structure based on comparison with the reported data (charmarite, Ref. code 00-051-1526). Reflexes belonging to MnCO<sub>3</sub> impurity are marked.

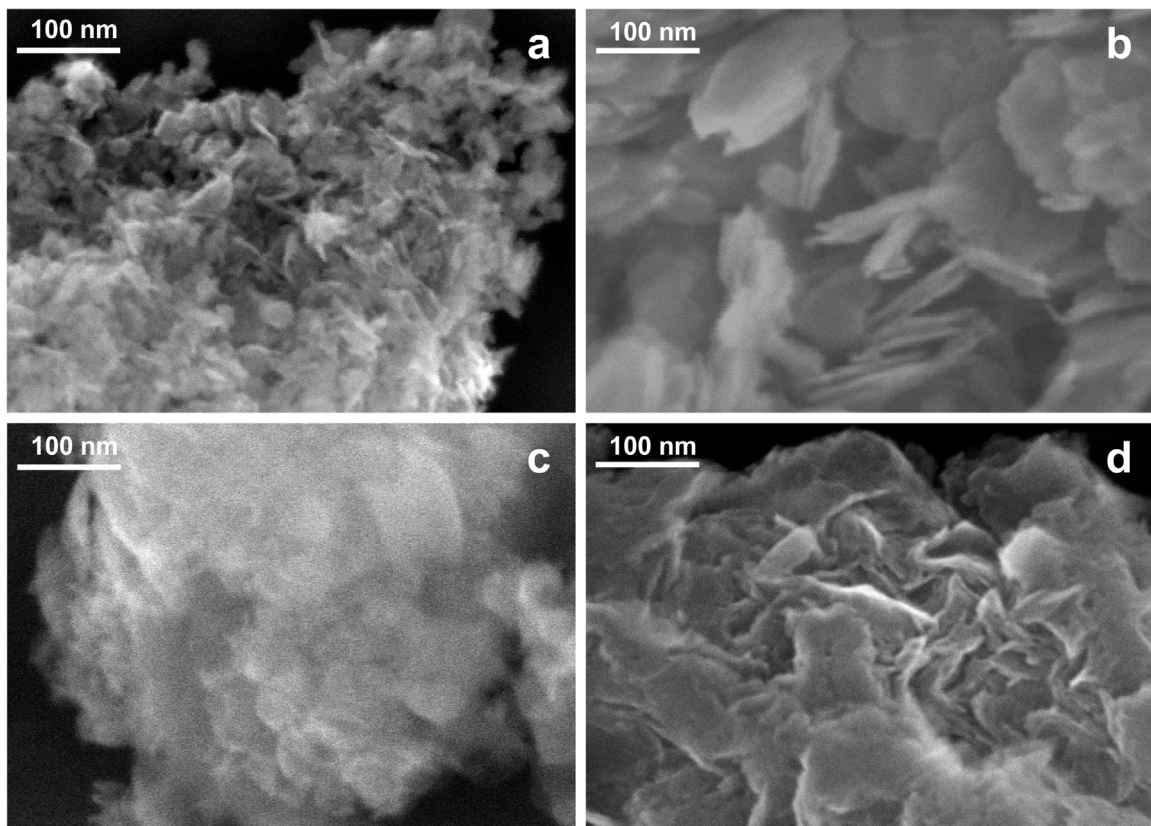


**Fig. 2.** SEM images of: (a) MnAl(im), (b) MnAl(st), (c) MnAl(im)/Na-L(II)-600, (d) MnAl(im)/CTA-L(II)-600 (uncoated specimens).

shows that combination of an organoclay dispersion in isopropanol with inverse micelles floating in isoctane leads to a higher degree of exfoliation of clay component than in the case of composites obtained from the aqueous dispersion of Laponite. Other XRD reflections present in calcined composites can be assigned to  $Mn_3O_4$ . Their appearance depends on the MnAl(im)/clay ratio, the temperature of calcination, and the manner of composites preparation. Thus, none of Na-L-based composites calcined at 450 °C shows any clear features of  $Mn_3O_4$ , which indicates that the Mn-containing oxide component is amorphous, similarly as in pure MnAl(im)-450 phase. In contrast, the MnAl(im)/CTA-L(II)-450 and MnAl(im)/CTA-L(III)-450 composites show evidence of hausmannite phase crystallization. Features assignable to  $Mn_3O_4$  are visible in all materials calcined at 600 °C, but, in general, are more pronounced in composites prepared from organo-clay. Thus, crystallization of hausmannite appears to be accelerated by the presence of CTA-L component. Explanation of this phenomenon is offered by comparison of thermal effects accompanying temperature programmed decomposition in air of Na-L and CTA-L based composites, illustrated by the example of uncalcined MnAl(im)/Na-L(II) and MnAl(im)/CTA-L(II) samples behavior (Fig. 4). The major difference between the DSC and TG profiles of both samples consists in the appearance of a strong exothermic effect with maximum between 260 and 290 °C, occurring in sample MnAl(im)/CTA-L(II) and absent in MnAl(im)/Na-L(II), associated with a significant mass loss in the 200–450 °C range. This phenomenon is related to the combustion of CTA cations present in organoclay component of the composite [30]. It is proposed that heat released during this reaction causes a local increase of temperature and enhances crystallization of the hausmannite phase in the calcined composites derived from organo-Laponite. The effect is similar to the long known formation of the so-called hotspots at the surface of the catalyst upon working in the exothermic reaction environment

[31]. Thermal phenomena above 750 °C, i.e. endothermic dehydroxylation of the Laponite layers, followed by a sharp exothermic effect due to the collapse of Laponite structure and recrystallization of amorphous meta-phases, are shifted to higher temperature in the organoclay-based material, which agrees with the previous study [30] and confirms that CTA-L is more stable than Na-L. Fig. 3 shows also the XRD pattern of reference MnAl(st)/Na-L(I)-600 sample, of similar Mn/Si ratio like MnAl(im)/Na-L(I)-600 composite, but prepared from MnAl(st) hydrotalcite obtained by the standard co-precipitation route. It is evident that reflections assignable to  $Mn_3O_4$  are much more pronounced, indicating better crystallinity of this phase, which is likely to be directly related to the larger particle size of the MnAl(st) precursor, as compared to the size of MnAl(im) grains (Fig. 2a, b). There is no evidence of an XRD-detectable Al-related oxide phase in any of the catalysts, which suggests an amorphous character of alumina and/or an Al-bearing mixed oxide phase.

Figs. 2b, c, and 5a, b show, respectively, SEM and TEM images of MnAl(im)/Na-L(II)-600 and MnAl(im)/CTA-L(II)-600 composites. From SEM data it is clear that the catalyst derived from organo-Laponite has a more loose, fluffy texture, than the one prepared from Na-L. This is in accordance with the XRD data implying better exfoliation of the organoclay component than the Na-L one. In TEM images of microtomed sections of composites embedded in the epoxy resin the manganese oxide component is visible as distinct grains in black and various shades of grey, dispersed among the randomly oriented Laponite particles. It is noticeable that in the MnAl/CTA-L(II)-600 composite (Fig. 5b), prepared in an organic environment, these grains are pretty uniform, of ca. 20–30 nm diameter, i.e. comparable with the basal size of the MnAl(im) platelets presented in Fig. 2a. On the other hand, in the MnAl/Na-L(II)-600 catalyst, obtained in aqueous medium, the size of manganese oxide particles is more diverse and bigger grains of up

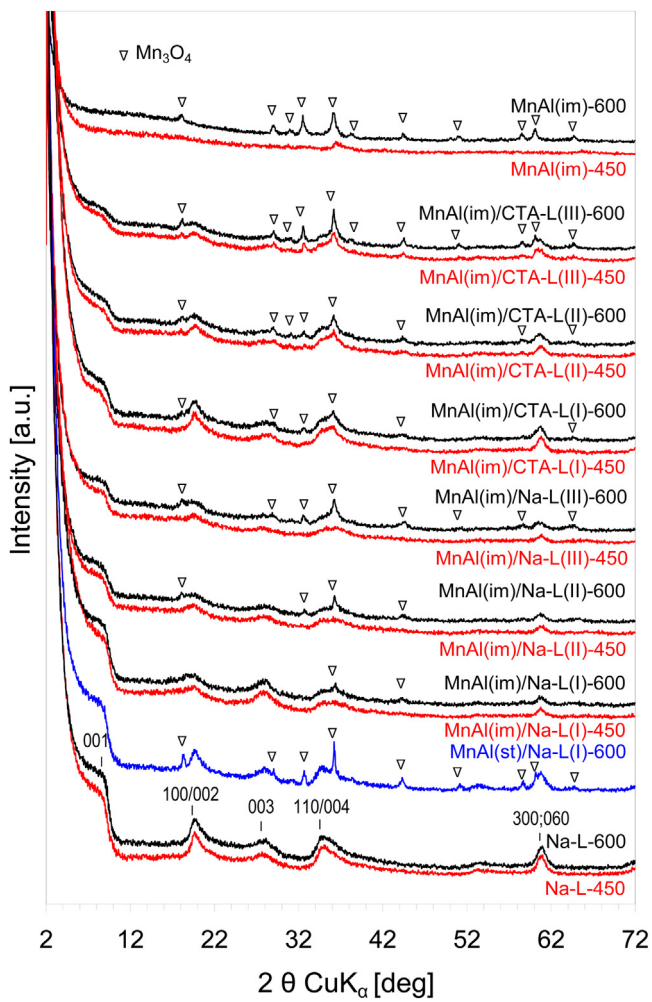


**Fig. 3.** XRD patterns of composite catalysts, MnAl(im) and Na-L, calcined at 450 and 600 °C. Indexing of Laponite based on comparison with the reported data (Ref. code 09-0031). Reflexes belonging to  $\text{Mn}_3\text{O}_4$  in samples calcined at 600 °C are marked.

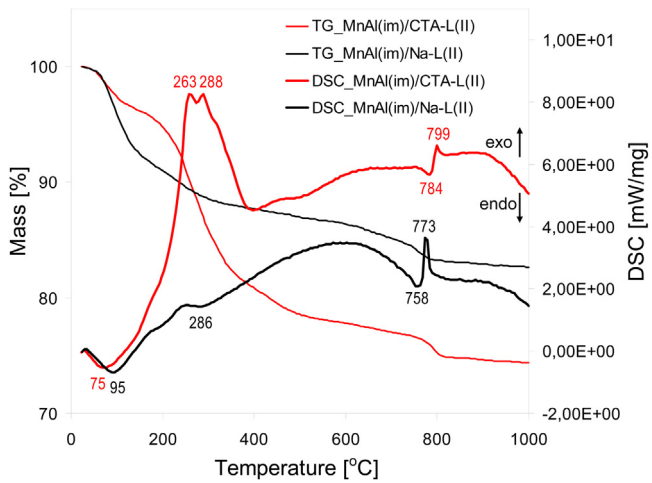


**Fig. 4.** Thermal analysis of uncalcined MnAl(im)/Na-L(II) and MnAl(im)/CTA-L(II) composites.

to 100 nm, presumably formed by coalescence of several MnAl(im) platelets appear next to the smaller ones (Fig. 5a). Fig. 5c and d shows, respectively, representative HRTEM images of manganese oxide particle in MnAl(im)/Na-L(II)-600 and MnAl(im)/CTA-L(II)-600 with visible lattice fringes. The corresponding SAED patterns

can be indexed to the [111] zone axis of  $\text{Mn}_3\text{O}_4$ . Reflections in diffraction pattern obtained from the  $\text{Mn}_3\text{O}_4$  nanocrystal belonging to MnAl(im)/CTA-L(II)-600 are sharper than those from the bigger oxide particle analyzed in MnAl(im)/Na-L(II)-600 sample. Thus, the  $\text{Mn}_3\text{O}_4$  phase present in MnAl(im)/CTA-L(II)-600, despite forming smaller grains, is better ordered than  $\text{Mn}_3\text{O}_4$  present in the bigger grains found in MnAl(im)/Na-L(II)-600. The result agrees with the findings of XRD analysis, which also point to better crystallinity of  $\text{Mn}_3\text{O}_4$  in composites obtained from CTA-L. As discussed before, the effect is attributed to the additional heat input form the combustion of the CTA cations during calcination of the organoclay-based material.

Thus, on the basis of the XRD and TEM data, the main difference between MnAl(im)/Na-L and MnAl(im)/CTA-L structures is that the latter are characterized by: (a) higher degree of Laponite exfoliation, (b) smaller and more uniform size of Mn oxide nanoparticles, and (c) more crystalline character of Mn oxide phase.

$\text{N}_2$  adsorption/desorption isotherms obtained for the MnAl(im)/Na-L and MnAl(im)/CTA-L series are presented in Fig. 6. It is visible that quantitative and qualitative differences exist between the two types of composite materials, but also that, for a given composite, the temperature of calcination does not affect the character of isotherm. The adsorption isotherms recorded for MnAl(im)/Na-L composites are of type IV, frequently observed for mesoporous adsorbents [32]. They all display a characteristic plateau/inflection at relative  $p/p_0$  close to saturation. The types of hysteresis loops in this series depend on the relative content of clay and mixed oxide component. In the case of MnAl(im)/Na-L(I) sample, with the least amount of MnAl oxide phase, the hysteresis loop may be described as H4, and indicates the presence of slit-shaped pores commonly found in powders composed of clay particles. Upon increase of MnAl oxide loading, for a given temperature of calcination, the adsorption capacity of MnAl(im)/Na-L composites increases, as indicated by the ever steeper character of the isotherms at higher  $p/p_0$ . For both temperatures of calcination, the desorption branches of MnAl(im)/Na-L(II) and MnAl(im)/Na-L(III) have a two-step profile, which leads to hysteresis loops with a complex shape, such as those reported for materials containing a contribution from mesopores with partially plugged passages [33–36]. The desorption step at higher relative pressure reflects emptying of open mesopores, while the blocked pores remain filled until the relative pressure drops below  $p/p_0 \sim 0.5$  and the cavitation of the nitrogen condensate leads to  $\text{N}_2$  desorption from the confined areas. In the most recent IUPAC classification such hysteresis loops have been referred to as type H5 [32]. All isotherms of MnAl(im)/CTA-L series are of type II with H3 hysteresis loops. The strong upward swing of these isotherms is the result of unrestricted monolayer-multilayer adsorption up to high  $p/p_0$ . As a result, all members of the MnAl(im)/CTA-L series display adsorption capacities much higher than those of the MnAl(im)/Na-L samples. Moreover, in contrast to the MnAl(im)/Na-L series, the positions of isotherms recorded for MnAl(im)/CTA-L samples are less affected by different compositions and by different calcination temperatures. As a consequence of such isotherms the textural parameters of MnAl(im)/Na-L and MnAl(im)/CTA-L series, presented in Table 2, show considerable differences. Thus, specific surface areas of calcined MnAl(im)/CTA-L samples are always larger than those of the corresponding MnAl(im)/Na-L composites, and their decrease upon calcination at higher temperature is less pronounced. Even more significant are the differences in total pore volumes, which for the MnAl(im)/CTA-L samples are much larger than for the MnAl(im)/Na-L counterparts. The effect is associated with larger average pore radii found in samples prepared from the organo-Laponite. Moreover, in the case of MnAl(im)/CTA-L samples the increase of calcination temperature from 450 to 600 °C leads to a slight increase of the total pore

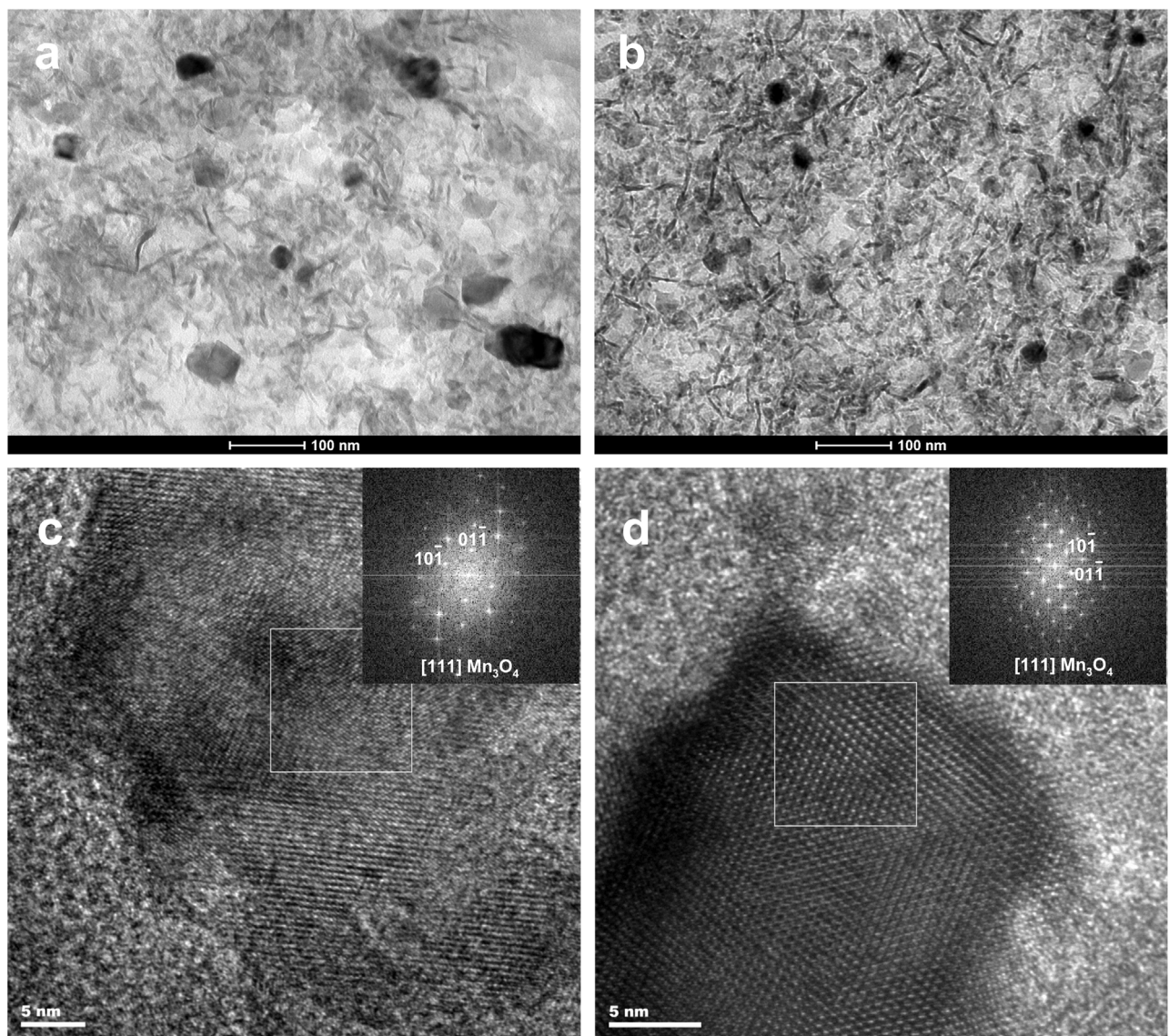


**Fig. 5.** (a) TEM image of MnAl(im)/Na-L(II)-600, (b) TEM image of MnAl(im)/CTA-L(II)-600, (c) HRTEM image of manganese oxide particle in MnAl(im)/Na-L(II)-600, with corresponding SAED pattern, (d) HRTEM image of manganese oxide particle in MnAl(im)/CTA-L(II)-600, with corresponding SAED pattern.

**Table 2**

Textural parameters, hydrogen consumption from TPR,  $T_{50}$ ,  $T_{90}$  and  $T_{90}-T_{50}$  from catalytic tests, MnAl(im)/Na-L and MnAl(im)/CTA-L series calcined at 450 and 600 °C.

Sample	$S_{\text{BET}}[\text{m}^2/\text{g}]$	$S_{\text{micro}}[\text{m}^2 \text{ g}^{-1}]$	$V_{\text{tot}}[\text{cm}^3 \text{ g}^{-1}]$	$V_{\text{micro}}[\text{cm}^3 \text{ g}^{-1}]$	$D^{\text{av}}[\text{\AA}]$	Isotherm	Loop	$H/\text{Mn}^{\text{TPR}}$	$T_{50}[\text{°C}]$	$T_{90}[\text{°C}]$	$T_{90}-T_{50}[\text{°C}]$
MnAl(im)/Na-L(I)-450	245	59	0.224	0.026	36.6	IV	H4	1.5	241	270	28
MnAl(im)/Na-L(I)-600	184	60	0.203	0.026	44.2	IV	H4	1.0	266	294	28
MnAl(im)/Na-L(II)-450	238	52	0.281	0.023	47.2	IV	H5	1.6	233	260	27
MnAl(im)/Na-L(II)-600	193	59	0.271	0.026	56.2	IV	H5	1.3	253	281	28
MnAl(im)/Na-L(III)-450	234	51	0.344	0.023	58.7	IV	H5	1.5	236	265	29
MnAl(im)/Na-L(III)-600	192	43	0.343	0.018	71.5	IV	H5	1.0	259	288	29
MnAl(im)/CTA-L(I)-450	303	41	0.462	0.018	61.0	II	H3	0.8	279	300	21
MnAl(im)/CTA-L(I)-600	286	43	0.515	0.018	72.0	II	H3	0.7	260	282	22
MnAl(im)/CTA-L(II)-450	296	34	0.478	0.014	64.5	II	H3	1.0	264	286	22
MnAl(im)/CTA-L(II)-600	271	35	0.524	0.014	77.3	II	H3	0.9	245	265	20
MnAl(im)/CTA-L(III)-450	262	26	0.502	0.011	76.6	II	H3	0.7	268	288	20
MnAl(im)/CTA-L(III)-600	231	28	0.513	0.011	88.8	II	H3	0.7	253	274	21
MnAl(st)/Na-L(I)-600	118	n.d.	n.d.	n.d.	n.d.	n.d.	n.d.	n.d.	290	352	62

volumes, while a decrease is observed MnAl(im)/Na-L samples. All samples are to some extent microporous, but microporosity is more pronounced in MnAl(im)/Na-L series (22–32% of the specific surface area) than in MnAl(im)/CTA-L materials (10–15% of the specific surface area). Summarizing, the composites derived from

organoclay are characterized by a more open pore network with no blocking, larger specific surface and pore volume, less sensitive to thermal degradation. It is likely that the presence of sodium in the materials obtained by the aqueous route contributes to the more facile degradation of their texture [37].

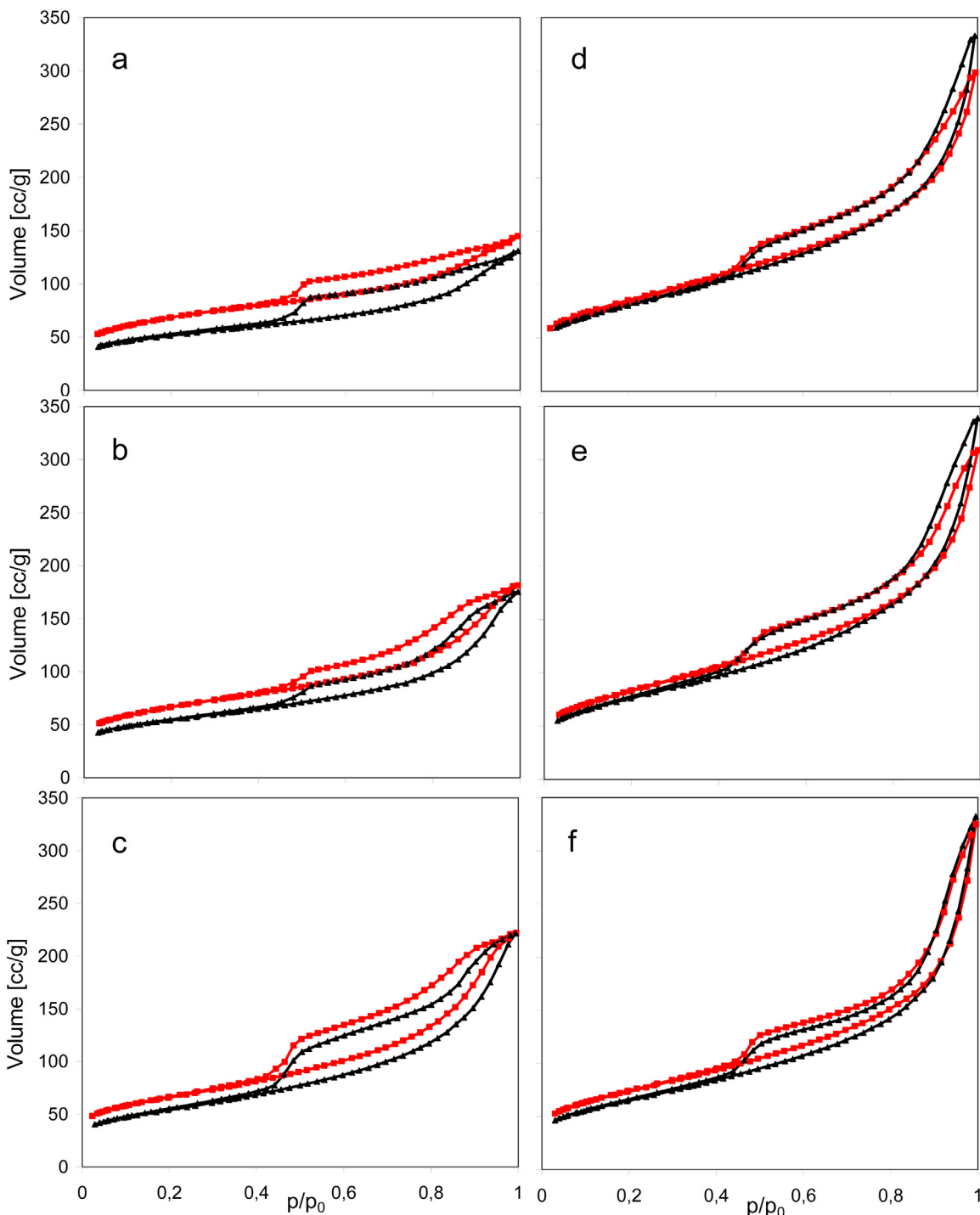


**Fig. 6.**  $\text{N}_2$  adsorption/desorption isotherms of (a) MnAl(im)/Na-L(I), (b) MnAl(im)/Na-L(II), (c) MnAl(im)/Na-L(III), (d) MnAl(im)/CTA-L(I), (e) MnAl(im)/CTA-L(II), (f) MnAl(im)/CTA-L(III), calcined at 450 (red lines) and 600 °C (black lines). (For interpretation of the references to colour in this figure legend, the reader is referred to the web version of this article.)

### 3.1.2. Redox properties

Reducibility of the Mn-containing active phase, an important factor determining activity in oxidation reactions, has been investigated by means of the temperature programmed reduction with hydrogen. The  $\text{H}_2$  TPR profiles of all investigated catalysts are presented in Fig. 7. All observed effects are associated with the Mn oxide phase, since in the investigated temperature range no hydrogen consumption is observed for the Laponite component. The sequence of effects observed upon reduction of manganese oxides is usually discussed in terms of the following successive

transformations:  $\text{MnO}_2 \rightarrow \text{Mn}_2\text{O}_3 \rightarrow \text{Mn}_3\text{O}_4 \rightarrow \text{MnO}$  [38]. In addition, different local environment around Mn sites in the same oxidation state may result in the appearance of more than one TPR maximum. Hausmannite, the only manganese oxide phase identified with XRD in the studied composites, has a normal spinel structure, of nominal composition  $\text{MnO} \bullet \text{Mn}_2\text{O}_3$ , with  $\text{Mn}^{2+}$  in the tetrahedral and  $\text{Mn}^{3+}$  in the octahedral sites. Therefore, if  $\text{Mn}_3\text{O}_4$  were the only form of  $\text{MnO}_x$  present in the composites, a single  $\text{H}_2$  consumption maximum would be expected, corresponding to the reduction of  $\text{Mn}^{3+}$  component of this phase to  $\text{Mn}^{2+}$  [38]. However,

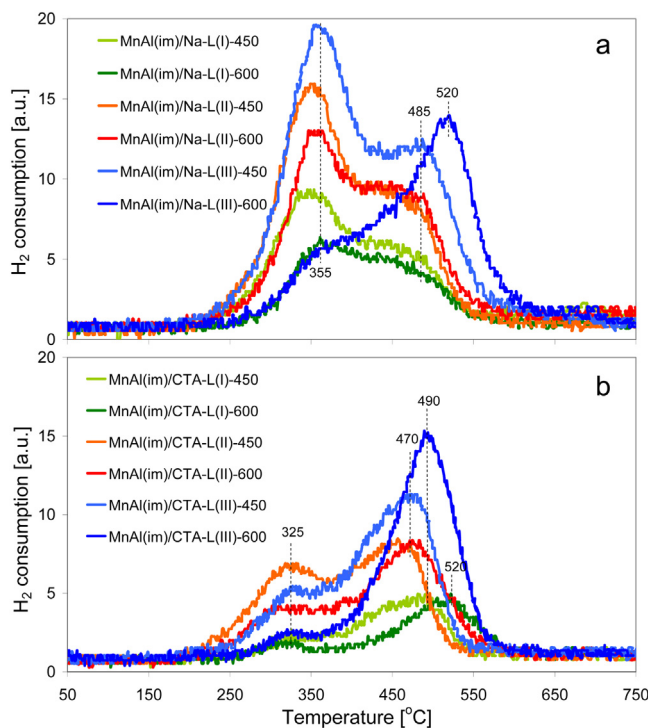


**Fig. 7.**  $\text{H}_2$  TPR profiles of (a)  $\text{MnAl}(\text{im})/\text{Na-L}$  composites (b)  $\text{MnAl}(\text{im})/\text{CTA-L}$  composites, calcined at 450 and 600  $^{\circ}\text{C}$ .

in all studied samples, beside the high temperature peak which, depending on the catalyst, appears in the range 450–520  $^{\circ}\text{C}$ , and may be assigned to  $\text{Mn}_3\text{O}_4$  reduction, a low temperature maximum is observed around 325  $^{\circ}\text{C}$  in  $\text{MnAl}(\text{im})/\text{CTA-L}$  series and around 355  $^{\circ}\text{C}$  in  $\text{MnAl}(\text{im})/\text{Na-L}$  samples. Yongnian et al. [39], who studied redox behaviour of trimanganese tetroxide catalysts, assigned the low temperature peak to the reduction of an oxygen-rich non-stoichiometric  $\text{Mn}_3\text{O}_4$  phase. However, in the present study the effect may also originate from reduction of  $\text{MnO}_2$ -like species, of crystallinity too low for detection by XRD. Comparison of TPR profiles in Fig. 7a and b shows that the overall  $\text{H}_2$  consumption by members of the  $\text{MnAl}(\text{im})/\text{Na-L}$  series is larger than that observed for the CTA-L based counterparts. This is mainly due to the fact that the low temperature maximum is much more pronounced in composites obtained from Na-L (Fig. 7a) than in composites derived from organoclay (Fig. 7b). In both types of composites an increase of the calcination temperature diminishes the low temperature maximum. If  $\text{Mn}_3\text{O}_4$  were the only Mn oxide phase, the overall hydrogen consumption should correspond to 0.66 H atoms per Mn center. The actual values approach this figure only in the case of  $\text{MnAl}(\text{im})/\text{CTA-L}$  series, for which the H/Mn ratio is in the range 0.7–1 (Table 2). The amount of hydrogen consumed by  $\text{MnAl}(\text{im})/\text{Na-L}$  calcined at 450  $^{\circ}\text{C}$  samples is ca. 1.5–1.6H/Mn, which is much more than the value expected for  $\text{Mn}_3\text{O}_4$ , or even  $\text{Mn}_2\text{O}_3$  (H/Mn = 1) and points to the contribution from species of  $\text{MnO}_2$ -like stoichiometry (H/Mn = 2). In samples calcined at 600  $^{\circ}\text{C}$  the H/Mn ratio falls to 1–1.3, but is still clearly higher than that expected for  $\text{Mn}_3\text{O}_4$ . Such a result implies that while the XRD detectable Mn oxide appears as  $\text{Mn}_3\text{O}_4$ , the amorphous component, particularly abundant in  $\text{MnAl}(\text{im})/\text{Na-L}$ -450 samples, contains significant amounts of  $\text{Mn}^{4+}$  and is of  $\text{MnO}_2$ -like stoichiometry. Indeed, the overall TPR profiles of the catalysts from the Na-L based series resemble those reported for  $\text{MnO}_2$  powders [40]. In such materials the first, more intense maximum is attributed to the concurrent reduction of  $\text{MnO}_2$  to  $\text{Mn}_2\text{O}_3$  and  $\text{Mn}_2\text{O}_3$  to  $\text{Mn}_3\text{O}_4$ , while the maximum at higher temperature corresponds to the reduction of  $\text{Mn}_3\text{O}_4$  to  $\text{MnO}$ .

The observed fall of the low temperature maximum intensity upon increase of the calcination temperature is consistent with the fact that at higher temperature  $\text{MnO}_2$  species undergo thermal decomposition to lower valent  $\text{Mn}_2\text{O}_3$  [41]. It should be noted that the low temperature TPR maximum in the  $\text{MnAl}(\text{im})/\text{CTA-L}$  series appears at 325  $^{\circ}\text{C}$ , which is significantly lower than 355  $^{\circ}\text{C}$  characterizing the position of the low temperature peak in Na-L based samples. Such a shift points not only to the better reducibility of part of Mn species present in the organoclay derived materials, but may be taken as an indication of a different environment around the Mn sites responsible for the low temperature effect. It may be speculated that while the low temperature hydrogen consumption in  $\text{MnAl}(\text{im})/\text{Na-L}$  catalysts is chiefly due to the reduction of amorphous  $\text{MnO}_2$ -like phase, in the  $\text{MnAl}(\text{im})/\text{CTA-L}$  it is largely due to the reduction of an oxygen-rich nonstoichiometric  $\text{Mn}_3\text{O}_4$  phase, as proposed by Yongnian et al. [39].

In order to further characterize the Mn-bearing component of the composite catalysts, selected samples calcined at 600  $^{\circ}\text{C}$  have been subjected to the XPS analysis of surface composition. Dispersion of the Mn-containing phase with respect to the silicate component can be assessed by comparison of the surface Mn/Si ratio obtained from the survey scan spectrum with that of the bulk value (Table 1). In all investigated samples the surface Mn/Si ratio is lower than the bulk one, which is consistent with the formation of grains of manganese oxide phase, rather than uniform spreading of Mn species over the silicate component. The electrons excited from the interior of such grains have smaller probability of surviving at the peak energy, and contribute to a lesser extent to the Mn spectrum intensity [42]. Moreover, it can be noticed that for a given level of doping with Mn (I or II), the surface Mn/Si ratio is always higher in  $\text{MnAl}(\text{im})/\text{CTA-L}$  composites. This confirms the conclusion, drawn from the results of TEM analysis, that dispersion of the Mn oxide phase is better in the catalysts prepared from organoclay. Analysis of Mn/Al surface ratio shows that it is always lower than the bulk value, the difference being more pronounced for the catalysts based on Na-L, containing bigger  $\text{MnO}_x$  particles. Such a result shows that upon thermal decomposition of the hydrotalcite-like precursor most, if not all, aluminium forms a separate oxide phase, better dispersed than the  $\text{MnO}_x$  oxide grains. Contribution of various Mn oxidation states has been calculated by employing the fitting procedure proposed by Nesbitt and Banerjee [43], taking into account the multiplet splitting. Fig. 8 illustrates, as an example, the deconvolution of Mn 2p spectra for  $\text{MnAl}(\text{im})/\text{Na-L}$ (II)-600 and  $\text{MnAl}(\text{im})/\text{CTA-L}$ (II)-600 samples. Lower signal to noise ratio for the latter reflects the better dispersion of Mn oxide phase. Analysis shows that, next to  $\text{Mn}^{3+}$  and  $\text{Mn}^{2+}$ , also  $\text{Mn}^{4+}$  species exist at the catalysts surface, as indicated already by the results of TPR experiments. It should be noted that even in the case of pure  $\text{Mn}_3\text{O}_4$ , past XPS studies indicated that the actual surface composition is close to 2  $\text{MnO} \bullet \text{MnO}_2$  rather than  $\text{MnO} \bullet \text{Mn}_2\text{O}_3$ . Although such a disproportionation explains the appearance of  $\text{Mn}^{4+}$ , it does not change the average oxidation state of Mn, which, for  $\text{Mn}_3\text{O}_4$  is 2.66. The data on the contribution of various Mn oxidation states, presented in Table 1, show that the surface of Na-L based materials is, in general, more oxidized than that of organoclay-derived catalysts. The average oxidation state is 3.1 for the former, and 2.8–2.9 for the latter. Both values are higher than 2.66 expected for  $\text{Mn}_3\text{O}_4$ , the only crystalline phase detected in materials calcined at 600  $^{\circ}\text{C}$ , but the difference is less pronounced for the  $\text{MnAl}(\text{im})/\text{CTA-L}$  samples. The latter samples show also a much higher content of  $\text{Mn}^{2+}$  than the  $\text{MnAl}(\text{im})/\text{Na-L}$  catalysts. This suggests, that in organoclay derived composites calcined at 600  $^{\circ}\text{C}$ , the manganese oxide phase crystallizes as an oxygen-rich, nonstoichiometric  $\text{Mn}_3\text{O}_4$ . On the other hand, in Na-L based catalysts, in which crystallization of trimanganese tetroxide is slower, the surface, next to  $\text{Mn}_3\text{O}_4$  grains, contains still an  $\text{MnO}_2$ -related amorphous component. Thus, the

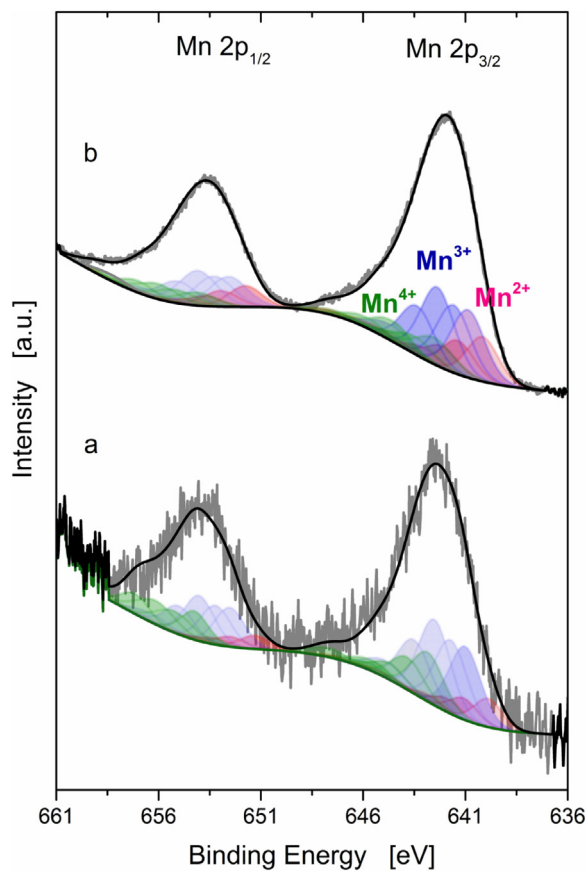


**Fig. 8.** Deconvolution of Mn 2p spectra for (a) MnAl(im)/Na-L(II)-600 and (b) MnAl(im)/CTA-L(II)-600 samples.

XPS data corroborate the TPR results as to the nature of the MnO<sub>x</sub> phase components.

Good reducibility is a key factor in determining the activity of an oxide phase in total oxidation reactions. Comparison of the redox properties of both types of composites shows that while in the Na-L derived catalysts the content of Mn<sup>4+</sup> species existing within the amorphous phase with MnO<sub>2</sub>-like stoichiometry is higher than the amount of Mn<sup>4+</sup> present at the oxygen-rich surface of Mn<sub>3</sub>O<sub>4</sub> crystallites in the organoclay-based composites, the latter are more reducible than the former. Both factors may be of importance for understanding of the catalytic patterns in the total oxidation of toluene.

### 3.2. Catalytic tests

Catalytic activity of calcined samples was tested in the reaction of total combustion of toluene. All investigated catalysts showed high activity, and the only reaction products were carbon dioxide and water. Fig. 9a shows the toluene ignition curves of the MnAl(im)/Na-L series, Fig. 9b gathers the corresponding data for MnAl(im)/CTA-L catalysts. For each series the catalytic performances of materials calcined at 450 and 600 °C are compared. In addition, in Fig. 9a, the data obtained for the reference MnAl(st)/Na-L(I)-600 sample are presented. It is obvious that the activities of both types of composites whose active phase was prepared from MnAl(im) hydrotalcite component are higher than that of the reference catalyst prepared with conventionally synthesized MnAl(st) hydrotalcite. This confirms the advantage of the general strategy of catalyst design based on trapping of MnAl(im) hydrotalcite nanoparticles between the clay layers.

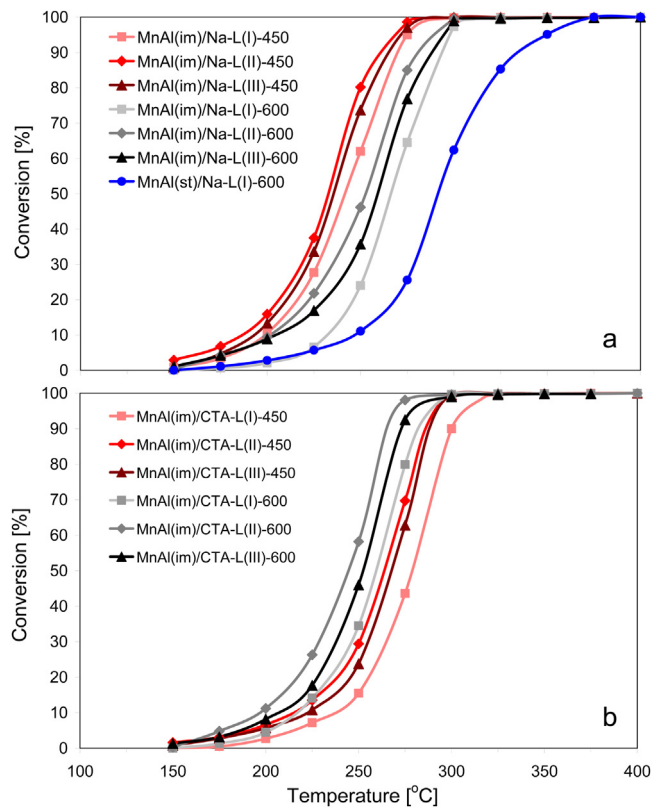


**Fig. 9.** Ignition curves for toluene combustion over (a) MnAl(im)/Na-L composites (b) MnAl(im)/CTA-L composites, calcined at 450 and 600 °C.

Analysis of Fig. 9 and comparison of the temperatures at which 50% (T<sub>50</sub>) and 90% (T<sub>90</sub>) toluene conversion is reached (Table 2) leads to some interesting observations. In the case of catalysts calcined at 450 °C, all MnAl(im)/Na-L composites show catalytic activity significantly higher than the MnAl(im)/CTA-L series. For Na-L based catalysts the T<sub>50</sub> values are by 31–40 °C below those of the corresponding MnAl(im)/CTA-L-450 samples, and the lowering of T<sub>90</sub> varies between 23 and 30 °C. The higher activity of the MnAl(im)/Na-L-450 series, despite lower specific surfaces and pore volumes, points to the crucial role of the higher average oxidation state of Mn in the amorphous MnO<sub>x</sub> active phase present in this series, which contains significantly more Mn<sup>4+</sup> than the more crystalline one found in MnAl(im)/CTA-L-450 catalysts. Calcination at 600 °C affects the catalytic performance of both types of composites, albeit in a totally different manner. In the case of the MnAl(im)/Na-L-600 series the result is not surprising, as the catalysts subjected to thermal treatment at higher temperature lose some of their activity. The increase of T<sub>50</sub> and T<sub>90</sub> is in the range 20–25 °C and 23–24 °C, respectively. In contrast, calcination at 600 °C has an unexpected positive effect on the performance of the MnAl(im)/CTA-L catalysts, as it significantly improves their performance with respect to the materials calcined at lower temperature. The lowering of T<sub>50</sub> when passing from MnAl(im)/CTA-L-450 to MnAl(im)/CTA-L-600 ranges from 20 to 25 °C and that of T<sub>90</sub> from 21 to 24 °C. This means that the related conversion profiles shift towards lower temperatures roughly by the same value as those of Na-L based catalysts move in the opposite direction. As a result, after calcination at higher temperature it is the MnAl(im)/CTA-L-600 series that shows the superior performance: the T<sub>50</sub> and T<sub>90</sub> values are, respectively, by 6–8 °C and 12–16 °C higher than those observed for the MnAl(im)/Na-L-600. The difference is more pronounced when comparing the T<sub>90</sub> values, because the characteristic feature of organoclay-based catalyst are the steeper profiles

of light-off curves, as indicated by the smaller difference between  $T_{90}$  and  $T_{50}$  values (Table 2). In an additional experiment the MnAl(im)/CTA-L-600(II) composite, best performing after calcination at 600 °C, was tested for stability by subjecting the catalyst to 24 h reaction run at temperature of 50% conversion. Within this period no deactivation was observed and the toluene conversion remained at the same level.

The observed dissimilar behaviour of two types of investigated composites suggests a complex interplay of various factors in shaping their catalytic performance. Upon increase of the temperature of calcination from 450 to 600 °C, the enhancement of sintering phenomena, leading to the coalescence of small active phase particles into larger ones, and causing fall of the catalyst activity, may be expected [23–25]. As discussed earlier, the analysis of  $S^{\text{BET}}$  and pore volumes of the composites shows that these phenomena affect to a much higher extent the catalysts derived from Na-L, which points to the degradation of texture as one reason for the observed loss of catalytic activity in this series. The other factor likely to affect adversely the catalytic activity of MnAl(im)/Na-L composites upon increase of the calcination temperature, is the fall of Mn<sup>4+</sup> content, due to the gradual evolution of Mn<sub>3</sub>O<sub>4</sub> phase from the amorphous MnO<sub>x</sub> material. In contrast, the organoclay based catalysts subjected to calcination at 600 °C retain ca. 90% of specific surface area displayed after thermal treatment at 450 °C, and their total pore volume shows even a slight increase. Thus, the MnAl(im)/CTA-L composites appear pretty immune to thermal degradation, so that deactivation due to sintering should not be a problem. While this explains why no loss of activity occurs in MnAl(im)/CTA-L composites after calcination at higher temperature, it still does not justify the observed activity increase. With the use of organoclays, one has to consider the possibility that in catalysts calcined at 450 °C some remnants of organic matter still exist, and are removed only after calcination at 600 °C, leading to the improvement of the catalytic performance. However, thermal analysis data presented in Fig. 4 show that maximum of the exothermic effect associated with the combustion of organic matter appears below 300 °C, i.e. much lower than the 450 °C used for calcination. Moreover, neither the TG/DSC of calcined MnAl(im)/CTA-L-450 composites bear any evidence of an exothermic effect which might be attributed to the combustion of the remaining organic matter, nor the FTIR analysis reveals any bands assignable to an organic deposit (data not shown). The ease of complete oxidation of the organic matter at relatively low temperature has been already observed in FeO<sub>x</sub>-containing organoclays, and attributed to the catalytic role of FeO<sub>x</sub> species [44]. In the materials studied in the present work, the efficient removal of the organic part of the composite is due to the catalytic action of the MnO<sub>x</sub> active phase dispersed between the clay layers. In view of this, it seems that the improved performance of the organoclay-based catalysts after increase of the calcination temperature is associated with the thermally induced evolution of Mn oxide phase, which is different for the two types of investigated composites, and leads to different forms of the MnO<sub>x</sub> active phase. Physicochemical characterization of the catalysts shows that in the case of organoclay-based composites formation and crystallization of uniformly sized nanoparticles of Mn<sub>3</sub>O<sub>4</sub> is favoured. Transformation of MnO<sub>x</sub> oxide phase into trimanganese tetroxide occurs also in composites obtained via the aqueous route, but the process is slower, the resulting active phase particles are less regular and, on average, bigger, and the evolving Mn<sub>3</sub>O<sub>4</sub> less crystalline. It has been shown that in the case of bulk MnO<sub>x</sub>, calcination in the temperature range used in this study should lead to the evolution of Mn<sub>2</sub>O<sub>3</sub> rather than Mn<sub>3</sub>O<sub>4</sub> [45]. However, it is also known that the phase interrelations in the MnO<sub>x</sub> system are size-dependent, and in smaller particles evolution of Mn<sub>3</sub>O<sub>4</sub> is favored, due to the lower surface energy of this phase [46]. In view of this, the preferred formation of uniform, well ordered Mn<sub>3</sub>O<sub>4</sub> nanocrystals in

MnAl(im)/CTA-L composites, as opposed to the less structurally ordered and size-wise diverse particles formed in MnAl(im)/Na-L composites, can be attributed to: (a) efficient dispersion of the MnAl(im) precursor grains between the organoclay particles, preventing coalescence of MnO<sub>x</sub> upon the composite calcination and enabling retention of the small particle size resulting from inverse micelle spatial constraints, (b) more facile transformation to Mn<sub>3</sub>O<sub>4</sub> due to the smaller size of MnO<sub>x</sub> particles, (c) additional heat input due to the exothermic effects accompanying combustion of the organic phase. It appears that the cooperation of the above factors leads to the formation of the active phase with unique properties, and suggests that the well ordered Mn<sub>3</sub>O<sub>4</sub> uniform nanocrystals with oxygen-rich surface, present in MnAl(im)/CTA-L-600 series, are more active than the less crystalline and richer in Mn<sup>4+</sup> manganese oxide phase formed after calcination of members of this series at 450 °C. An important factor likely to contribute to the excellent catalytic performance of MnAl(im)/CTA-L catalysts after calcination at 600 °C is that the surface Mn<sup>4+</sup>-rich layer of Mn<sub>3</sub>O<sub>4</sub> nanocrystals retains enhanced reducibility. The obtained results demonstrate the potential of using organoclays as supports for the active oxide phase prepared from inverse micellar precursors. On one hand the organic interlayer facilitates dispersion of the micelles between the clay layers, and, on the other, offers the unique opportunity of enhancing crystallization of uniform oxide nanoparticles during calcination, due to exothermic effects associated with combustion of the organic components of the system. In addition, the observed good textural stability of organoclay based composites upon high temperature treatment, combined with the improvement of their catalytic activity on increase of the calcination temperature, renders the materials particularly attractive for design of robust VOCs combustion catalysts.

#### 4. Conclusions

The general strategy of catalyst design based on trapping of MnAl hydroxylate nanoparticles obtained by inverse microemulsion between the Laponite clay layers proved successful and yielded VOCs combustion catalysts more active than the reference prepared from MnAl hydroxylate synthesized by a standard coprecipitation. Characterization of the composite catalysts revealed that the degree of clay exfoliation is higher in materials obtained from organo-Laponite than in the catalysts prepared from the sodium form of clay. Also, MnO<sub>x</sub> particles are more uniform and better dispersed in the former. The composition of MnO<sub>x</sub> active oxide phase is different for the two types of investigated composites. In MnAl(im)/CTA-L samples the MnO<sub>x</sub> component evolves towards well ordered, slightly oxygen-rich Mn<sub>3</sub>O<sub>4</sub> nanocrystals, while in MnAl(im)/Na-L materials the less structurally ordered and size-wise diverse particles are formed, of average oxidation state significantly higher than that characteristic of Mn<sub>3</sub>O<sub>4</sub>. It is postulated that the less abundant but more reducible Mn<sup>4+</sup> species found in organoclay-based composites belong mainly to the oxygen-rich surface of Mn<sub>3</sub>O<sub>4</sub> crystallites, while the less reducible ones present in Na-L derived catalysts exist within the amorphous phase with MnO<sub>2</sub>-like stoichiometry. Composites based on Na-L are more susceptible to thermal degradation, and lose activity when passing from calcination temperature 450–600 °C. In contrast, the organoclay-based catalysts improve their performance on the increase of the calcination temperature, due to favorable compositional and structural evolution of the active phase, and, as a result, after pretreatment at 600 °C, perform better than their counterparts obtained via the aqueous route. This effect, combined with good textural stability of organoclay based composites upon high temperature treatment, makes them very promising materials for design of robust VOCs combustion catalysts. The result

underlines the advantages of the proposed novel strategy of catalyst design, based on the use of organoclays in combination with transition metal containing hydrotalcite-like active phase precursors formed within the inverse micelles. This approach, on one hand, facilitates dispersion of the hydrotalcite precursor seeds and prevents the occurrence of active phase coalescence, on the other, provides interlayer fuel for the additional heat input during calcination, enabling formation of well ordered, uniform, transition metal oxide nanocrystals. In addition, the proposed catalyst design offers means of controlling the size of active phase particles by the appropriate choice of the inverse microemulsion synthesis parameters, thus opening yet another route for catalyst optimization. In view of the documented role of well defined nanocrystalline phases in a variety of catalytic processes [47], the catalysts designed according to the general procedure described in our work are likely to find application beyond the scope of the total oxidation reactions.

## Acknowledgment

This work was supported financially by the Polish National Science Center (NCN) grant OPUS 2013/09/B/ST5/00983.

## References

- [1] J.J. Spivey, Ind. Eng. Chem. Res. 26 (1987) 2165–2180.
- [2] W.B. Li, J.X. Wang, H. Gong, Catal. Today 148 (2009) 81–87.
- [3] H. Huang, Y. Xu, Q. Feng, D.Y.C. Leung, Catal. Sci. Technol. 5 (2015) 2649–2669.
- [4] A. Vaccari, Catal. Today 41 (1998) 53–71.
- [5] M. Zimowska, A. Michalik-Zym, R. Janik, T. Machej, J. Gurgul, R.P. Socha, J. Podobiński, E.M. Serwicka, Catal. Today 119 (2007) 321–326.
- [6] R. Dula, R. Janik, T. Machej, J. Stoch, R. Grabowski, E.M. Serwicka, Catal. Today 119 (2007) 327–331.
- [7] J.F. Lamonier, A.B. Boutoundou, C. Gennequin, M.J. Pérez-Zurita, S. Siffert, A. Aboukais, Catal. Lett. 118 (2007) 165–172.
- [8] K. Jirátová, J. Mikulová, J. Klempa, T. Grygar, Z. Bastl, F. Kovanda, Appl. Catal. A 361 (2009) 106–116.
- [9] L.A. Palacio, J. Velásquez, A. Echavarría, A. Faroc, F.R. Ribeiro, M.F. Ribeiro, J. Hazard. Mater. 177 (2010) 407–413.
- [10] D.A. Aguilera, A. Perez, R. Molina, S. Moreno, Appl. Catal. B 104 (2011) 144–150.
- [11] F. Kovanda, K. Jirátová, Appl. Clay Sci. 53 (2011) 305–316.
- [12] F. Kovanda, K. Jirátová, Catal. Today 176 (2011) 110–115.
- [13] E. Genty, R. Cousin, S. Capelle, C. Gennequin, S. Siffert, Eur. J. Inorg. Chem. (2012) 2802–2811.
- [14] F. Kovanda, K. Jirátová, J. Ludvíková, H. Raabová, Appl. Catal. A 464–465 (2013) 181–190.
- [15] T. Machej, E.M. Serwicka, M. Zimowska, R. Dula, A. Michalik-Zym, B. Napruszewska, W. Rojek, R. Socha, Appl. Catal. A 474 (2014) 87–94.
- [16] M.H. Castaño, R. Molina, S. Moreno, Appl. Catal. A 492 (2015) 48–59.
- [17] M. Jabłońska, L. Chmielarz, A. Węgrzyn, K. Góra-Marek, Z. Piwowarska, S. Witkowski, E. Bidzińska, P. Kuśtrowski, A. Wach, D. Majda, Appl. Clay Sci. 114 (2015) 273–282.
- [18] S. Mo, S. Li, W. Li, J. Li, S. Peng, J. Chen, Y. Chen, J. Mater. Chem. A 811 (2016) 3–811 (2).
- [19] L.M. Gandía, M.A. Vicente, A. Gil, Appl. Catal. B 38 (2002) 295–307.
- [20] A. Gil, M.A. Vicente, S.A. Korili, Catal. Today 112 (2006) 117–120.
- [21] T. Mishra, P. Mohapatra, K.M. Parida, Appl. Catal. B 79 (2008) 279–285.
- [22] M. Dhahri, M.A. Muñoz, M.P. Yeste, M.A. Cauqui, N. Frini-Srasra, React. Kinet. Mech. Catal. 118 (2016) 655–668.
- [23] J.J. Spivey, J.B. Butt, Catal. Today 11 (1992) 465–500.
- [24] P. Forzatti, L. Lietti, Catal. Today 52 (1999) 165–181.
- [25] J.A. Moulijn, A.E. van Diepen, F. Kapteijn, Appl. Catal. A: Gen. 212 (2001) 3–16.
- [26] W.B. Li, W.B. Chu, M. Zhuang, J. Hua, Catal. Today 93–95 (2004) 205–209.
- [27] F. Bellezza, A. Cipiciani, U. Costantino, M. Nocchetti, T. Posati, Eur. J. Inorg. Chem. 18 (2009) 2603–2611.
- [28] S. Aisawa, H. Hirahara, H. Uchiyama, S. Takahashi, E. Narita, J. Solid State Chem. 167 (2002) 152–159.
- [29] F. Cavaní, F. Trifirò, A. Vaccari, Catal. Today 11 (1991) 173–301.
- [30] H. Pálková, J. Madejová, M. Zimowska, E. Bielańska, Z. Olejniczak, L. Lityńska-Dobrzańska, E.M. Serwicka, Microporous Mesoporous Mater. 127 (2009) 228–236.
- [31] C. Steinbrüchel, L.D. Schmidt, Surf. Sci. 40 (1973) 693–707.
- [32] M. Thommes, K. Kaneko, A.V. Neimark, J.P. Olivier, F. Rodriguez-Reinozo, J. Rouquerol, K.S.W. Pure Appl. Chem. 879 (2015) 1051–1069.
- [33] P. Van Der Voort, P.I. Ravikovich, K.P. De Jong, A.V. Neimark, A.H. Janssen, M. Benjelloun, E. Van Bavel, P. Cool, B.M. Weckhuysen, E.F. Vansant, Chem. Commun. (2002) 1010–1011.
- [34] M. Kruk, M. Jaroniec, S.H. Joo, R. Ryoo, J. Phys. Chem. 107 (2003) 2205–2213.
- [35] E. Van Bavel, P. Cool, K. Aerts, E.F. Vansant, J. Phys. Chem. B 108 (2009) 5263–5268.
- [36] W. Wang, W. Shan, H. Ru, J. Mater. Chem. 21 (2011) 17433–17440.
- [37] V. Perrichon, M.C. Durupt, Appl. Catal. 42 (1988) 217–227.
- [38] F. Kapteijn, L. Singoredjo, A. Andreini, Appl. Catal. B 3 (1994) 169–173.
- [39] Y. Yongnian, H. Ruili, C. Lin, Z. Jiayu, Appl. Catal. A 101 (1993) 233–252.
- [40] X. Fu, J. Feng, H. Wang, K.M. Ng, Catal. Commun. 10 (2009) 1844–1848.
- [41] M.I. Zaki, M.A. Hasan, L. Pasupulety, K. Kumari, Thermochim. Acta 303 (1997) 171–181.
- [42] S. Tougaard, J. Electron Spectrosc. Relat. Phenom. 178–179 (2010) 128–153.
- [43] H.W. Nesbitt, D. Banerjee, Amer. Mineralog. 83 (1998) 305.
- [44] P. Natkański, P. Kuśtrowski, A. Białas, J. Surman, J. Therm. Anal. Calorim. 113 (2013) 335–342.
- [45] E.R. Stobbe, B.A. de Boer, J.W. Geus, Catal. Today 47 (1999) 161–167.
- [46] A. Navrotsky, C.C. Ma, K. Lilova, N. Birkner, Science 330 (2010) 199–201.
- [47] K. Zhou, Y. Li, Angew. Chem. Int. Ed. 51 (2012) 602–613.